Soft Matter

Accepted Manuscript

This is an *Accepted Manuscript*, which has been through the Royal Society of Chemistry peer review process and has been accepted for publication.

Accepted Manuscripts are published online shortly after acceptance, before technical editing, formatting and proof reading. Using this free service, authors can make their results available to the community, in citable form, before we publish the edited article. We will replace this *Accepted Manuscript* with the edited and formatted *Advance Article* as soon as it is available.

You can find more information about *Accepted Manuscripts* in the Information for Authors.

Please note that technical editing may introduce minor changes to the text and/or graphics, which may alter content. The journal's standard Terms & Conditions and the Ethical guidelines still apply. In no event shall the Royal Society of Chemistry be held responsible for any errors or omissions in this *Accepted Manuscript* or any consequences arising from the use of any information it contains.

ROYAL SOCIETY OF CHEMISTRY

www.rsc.org/softmatter

Journal Name

ARTICLE TYPE

Cite this: DOI: 10.1039/xxxxxxxxxx

Complex flow dynamics around 3D microbot prototypes

Sergio Martínez-Aranda, Francisco J. Galindo-Rosales and Laura Campo-Deaño*

Received Date
Accepted Date

DOI: 10.1039/xxxxxxxxxx

www.rsc.org/journalname

A new experimental setup for the study of the flow dynamics around 3D microbot prototypes in a straight microchannel has been developed. The ultimate aim of this work is focused on the analysis of the morphology of different microbot prototypes to get a better insight of their efficiency when they swim through the main conduits of the human circulatory system. The setup consists of a fused silica straight microchannel with a 3D microbot prototype fastened in the center of the channel cross-section by an extremely thin support. Four different prototypes were considered: a cube, a sphere and two ellipsoids with aspect ratios 1:2 and 1:4, respectively. Flow visualizations and micro-Particle Image Velocimetry (μPIV) measurements were performed using Newtonian and viscoelastic blood analogue fluids. An efficiency parameter, $\Im$, to discriminate the prototypes in terms of flow disturbance has been proposed.

1 Introduction

Microbots are mechanical or electromechanical devices whose components are at or close to the scale of micrometers. They have been developed for several purposes like industrial applications or biomedicine[1–3]. During the last two decades, some of the biggest technological advances have involved the use of theses microdevices in the area of biomedicine to perform precise and delicate tasks inside the human body, with the most impacting applications being related to their use as cancer-fighting microbots[4], to carry the drugs into the body[5] or as oxygen-sensing microbots to assess oxygen levels within the eye[6]. However, the manipulation and applicability of these microdevices is a challenging task and some technical issues must be solved[7], as they are their fabrication method, their propulsion mechanism, navigation and/or their dynamic efficiency when they move through the main conduits of the human body. This paper is focused on this latter issue, especially due to the combined effects of the viscoelastic character of the human biofluids and small length-scales of the flow paths.
The dimensionless numbers characterizing the viscoelastic fluid flows are the Reynolds number (Re), defined as the ratio between inertial and viscous forces, $Re = \rho UL/\eta$, and the Weissenberg number (Wi), which is the ratio between the relaxation time of the fluid and the characteristic time scale of the flow, $Wi = \lambda U/L$[8], where U represents the relative flow velocity, L the characteristic length-scale and ρ, λ and η are the density, relaxation time and viscosity of the fluid, respectively. In the human microcirculatory system, due to the small characteristic length scales, Wi increases as Re decreases, leading to enhanced elastic effects[9], which highlights the importance of treating blood flow as a non-Newtonian fluid. Blood exhibits non-Newtonian behaviour due to its complex mixture of proteins and of suspended cellular elements in plasma, like platelets, leucocytes and mainly erythrocytes[10,11]. The rheology of blood is strongly determined by the presence of red blood cells which are the responsible of its complex behaviour[10–16]. If blood is allowed to rest for several seconds, the red blood cells form aggregates, called rouleaux, and eventually create an interconnected network. When the rouleaux are broken up by shear and strain, a relative decrease in blood viscosity appears as shear rate is increased characteristic of shear-thinning behaviour, up to values around 100 s^{-1}.[16–19] However, the Newtonian approximation is still valid when high shear rates and large arteries or veins are considered. Nevertheless, as shown in recent studies[20,21], it has became evident the influence of the non-Newtonian properties of the fluid on the translating capabilities of micro-swimmers. Therefore, for these reasons the flow dynamics forces experienced by robots at the micro scale immersed in a biofluid are expected to be different from those experienced at the macroscale.
The manufacturing of microbots for their use in biomedicine entails several aspects, as they are the morphology, which can varies according to the function it has to perform; the biocompatibility with human fluids and conducts; and the power supplied for its movement. Most of these microbots are bio-inspired swimming microdevices that have been modeled inspired in bacteria or spermatozoa movement and propulsion. In this field, some research has been directed to the fabrication method of microbot proto-

CEFT, Faculty of Engineering, University of Porto. Rua Dr. Roberto Frias, 4200-465 Porto, Portugal. Fax: +351 22 508 1440; Tel: +351 22 508 1400. E-mail: (campo@fe.up.pt; laura@campodeano.com,)

† Electronic Supplementary Information (ESI) available: [details of any supplementary information available should be included here]. See DOI: 10.1039/b000000x/

types. Zeeshan et al.[22] reported the fabrication of an hybrid artificial bacterial flagella which reduces sedimentation and facilitate navigation and better biocompatibility in comparison with their metallic counterparts; Kim et al.[23] fabricated and characterized microbots based on 3D porous micro-niches as transported using a photo curable polymer; Suter et al.[24] fabricated swimming microbots made of magnetic polymer composite, which presented negligible cytotoxicity being suitable for biomedical applications. Other studies deal with the control motion and propulsion of these microdevices, mainly by the application of magnetic fields. Fountain et al.[25] used magnetic fields from a single rotating permanent magnet for the control of magnetic helical microbots which resulted in a viable option for wireless control of these kind of microbots; Solovev et al.[26] described the magnetic control of self-propelled microbots by an external magnetic field able to load and manipulate micro objects made of different kinds of materials and dispersed in a solution; Abbott et al.[27] compared different swimming methods commonly used in literature utilizing magnetic fields, they concluded that helical propellers are likely the best overall choice for *in vivo* applications; Belharet et al.[28] proposed a new technique for path finding, reconstruction and navigation control of a ferromagnetic microbot propelled with magnetic forces using magnetic resonance imaging; Palagi et al.[29] studied a propulsion mechanism inspired in the *metachronal waves* in ciliates to be applied in self-propelled swimming microbots; Peyer et al.[30,31] reviewed extensively the swimming mechanism of bacteria to model their motion and to fabricate artificial bacterial microbots; Felderhof[32] developed a numerical study about the self-propulsion of a electric or magnetic microbot in a polar viscous fluid, and more recently, Khalil et al.[33] studied and characterized the self-propulsion of a new microbot inspired in the propulsion system of a sperm-cell.

Works related to the improvement of the hardware architecture to a better transmission and communication were also developed in the last years. Sharafi et al.[34] described a technique based on binary communication scheme to communicate information from a microbot to an external computer; Corradi et al.[35] developed one of the smallest optic systems for communication and sensing of microbots, and Boillot et al.[36] presented a simulation framework for microbots using nano-wireless communication, among others.

However, experimental and numerical studies related to the characterization of the 3D fluid flow dynamics around the microbots are still missing. This analysis is of great importance to understand the influence of the microbot's morphology in the flow dynamics in order to improve their efficiency when they move through different conduits inside the human body, especially in the case of small vessels in the circulatory system, where non-Newtonian properties of blood are enhanced. To address this challenge, a new experimental setup has been designed, developed and validated. This setup consisted on a fused silica straight microchannel with a 3D microbot prototype fastened in the center of the channel cross-section by an extremely thin fused silica filament. Four different and simplified shapes of microbots were considered in this pioneering study following the most common geometries adopted for the currently developed bio-inspired microbots. Flow visualizations and μPIV were carried out to analyze the microhydrodynamics of the fluid flow around the different microbot's prototypes. Moreover, numerical simulations were performed in order to study the feasibility of the experimental setup (see Supporting Information).

Table 1 Shapes and dimensions of some experimental microbot prototypes.

Microbot Prototype	Main body shape	Dimensions [μm]
Mag-μBot[39,40]	Parallelepiped	100 x 130 x 250
OctoMag[41]	Elliptical	250 x 500
Paramagn. sphere[42,43]	Spherical	100
MagPieR[44]	Parallelepiped	230 x 300 x 388
Magn. sphere[45]	Spherical	500
Micro-jet[46]	Cylindrical	5 x 50
Porous microbot[23]	Cylindr.-Parallel.	75 x 75 x 150
MagnetoSperm[33]	Elliptical	30 x 50
Sphere-flagella[47,47,48]	Spherical	360
Parallel.-flagella[22]	Parallelepiped	5 x 10 x 20
Cylinder-flagella[48]	Cylindrical	400 x 800

2 Experimental setup

2.1 Microdevices design and fabrication

The flow conditions in the human body circulatory system present huge variations as the distance from the heart increases, from vessels having characteristic diameters of 2-3 mm and $Re \sim 3000$ close to the heart (considering the vessel diameter and the mean flow velocity as characteristic values), with a high pulsating component on the flow; to the smallest capillaries with characteristic diameters about 20-30 μm, $Re \leq 1$ and almost constant flow[37]. As mentioned previously, small length scales increase the significance of the viscoelastic nature of the human blood and, thus, we focus on medium to small size vessels (diameter $\leq$ 1 mm). Largely, blood consists of a Newtonian fluid named plasma, in which red blood cells measuring 5-10 μm in diameter and smaller platelets and white cells are suspended[38]. Therefore, in order to avoid discrete interactions between the real environment and the microbot device, we considered a lowest threshold of 10 times the red blood cells size for the minimum length of the microbots.

Table 1 shows the main features of the current prototypes reported in literature, together with their characteristic lengths. Based on them, we have considered for this study four different simplified microbot prototypes (hereafter refereed as models) having a common characteristic length-scale $R_1 = 50$ μm and varying from blunt to slender morphology: a 100 μm side cube (CU), a 100 μm diameter sphere (SP) and two 100μm minor axis ellipsoids with 200 μm (E2) and 400 μm (E4) major axis respectively. The models were orientated towards the flow direction and placed at the center of a square cross-section straight microchannel of 700 μm side length ($L_c = 350$ μm, where L_c is the characteristic length-scale of the channel). Therefore, the ratio between model and channel characteristic length-scales ($BR = R_1/L_c \sim 0.14$) is suitable to keep low-moderate blockage effects, in order to avoid an excessive influence of the channel walls on the model dynamics[49,50].

The models were fastened to the top-wall of the channel square

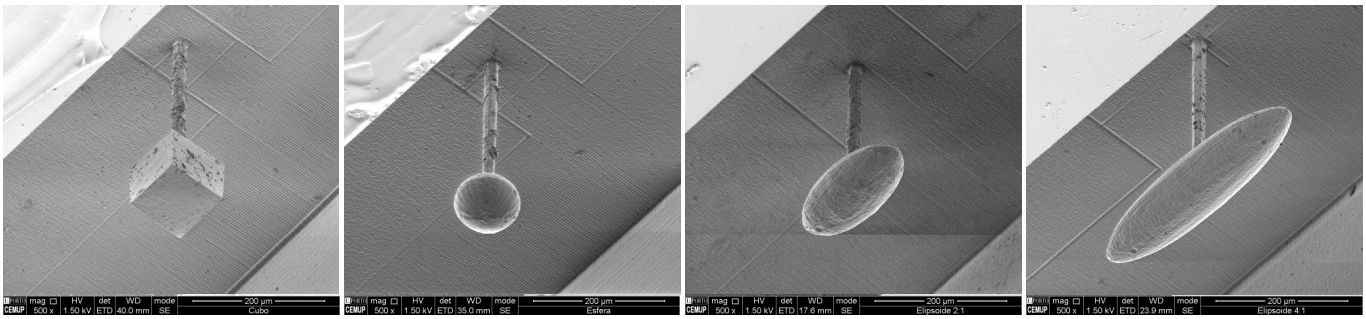

Fig. 2 Scanning electron microcope images of the four models fabricated. From left to right: cube, sphere, ellipsoid 1:2 and ellipsoid 1:4 prototypes.

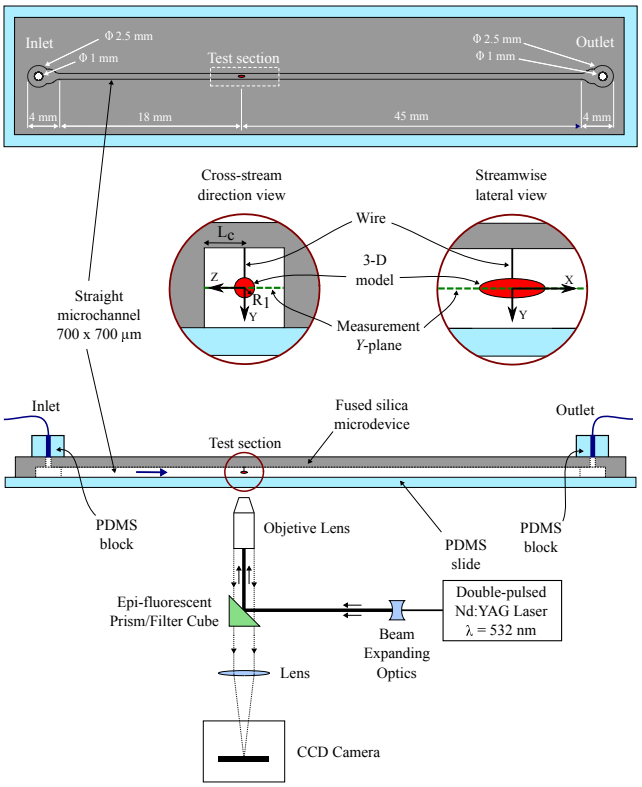

Fig. 1 Sketch of the micro-hydrotunnel and the experimental setup.

by means of a thin filament. This cylindrical support is 300 μm long and has a diameter of 20 μm. The support diameter selection was made based on previous fluid-structure interaction (FSI) simulations performed with a blood-like Newtonian steady flow and fully-elastic solid material assumption, in order to determine the optimal diameter able to satisfy two criteria: on one hand, resisting the forces exerted by the flow and avoiding fluctuations on the model position while the fluid circulates; on the other hand, minimizing the disturbance of the flow around the model. Support collapse probability was determined by means of the Tresca, Von-Mises, Rankine and Mohr-Coulomb fracture criteria. A minimum diameter of 20 μm was needed to ensure reaching Re = 150 in the microchannels without the support collapse for the most unfavorable case (results not shown here). The disturbance on the flow caused by the presence of this support is bellow 10% of the mean velocity in the channel, as it is thoroughly discussed in Supporting Information.

Fig. 1 depicts a scheme of the micro-hydrotunnel and the whole experimental setup. Straight microchannel was 63 mm long. In order to allow the flow becomes fully developed before reaching the test section and, thus, avoid any entry effects, the models were placed at a distace of 18 mm from the beginning of the straight channel. The distance from the center of the model to the end of the straight channel was 45 mm, long enough to allow the flow become fully developed again and avoid exit effects. Moreover, especial contraction-expansion sections were added at the beginning and at the end of the straight channel to provide a smoother flow transition at the inlet and outlet of the microchannel, respectively, as it is typically done at the inlet of the macroscale hydro-aerodynamics tunnels[51].

The bottom side of the microdevice was sealed with a polydimethylsiloxane (PDMS) slide of ∼1 mm thickness. Moreover, PDMS blocks of ∼5 mm thickness were also used to cover the inlet and outlet holes and hold the dispensing tips connecting the tubes. The microbot prototype, the support and the microchannel were fabricated all together from a unique bulk piece of fused silica, ensuring mechanical continuity. A new technology, recently developed by *Femtoprint, S.A* and based on the application of an ultra-fast low power femtosecond laser to the fused silica substrate, was used to fabricate these devices. Focused inside the glass, this laser locally modifies the refractive index of the material and increases the etching rate, resulting on a 3D micropattern without a mask process. Then this micro-pattern is developed by a chemical wet etching process, creating the model, filament and microchannel wall surfaces all together in the same bulk substrate slide. Fig. 2 shows Scanning Electron Microscope (SEM) images of the four models fabricated. Accuracy on dimensions is lower than 1 μm for the model and the filament. Model surface roughness was ∼200 nm depth.

2.2 Rheology of blood analogue fluids and flow regimens

Newtonian and viscoelastic blood analogues were prepared and used as working fluids. The Newtonian blood analogue consists of an aqueous solution of 68% w/w of dimethylsulfoxide (DMSO)[52,53], having a density of 1.135 g/cm^3. The viscoelastic blood analogue was formulated according to Campo-Deano et al.[15], consisting of a mixture of 100 ppm of xantham gum in an aqueous solution of 52% w/w of DMSO, having a density of 1.130 g/cm^3. Moreover, 50 ppm of sodium azide were added

in order to avoid the growth of microorganisms. Densities were measured averaging three test performed with a 10 ml pycnometer at a stable room temperature of ∼20 °C. The viscosity curve of both working fluids has been measured at steady shear rates ranging from 1 to 25000 s^{-1} by using a stress controlled rotational rheometer Anton Paar Physica MCR-301 and a 50 mm plate-plate geometry with a gap of 100 μm (Fig. 3). The Newtonian blood analogue fluid showed a constant viscosity of 3.80 mPa·s at 20 °C. The viscoelastic solution presented shear-thinning behavior with a plateau viscosity of 3.75 mPa·s at high shear-rates (20 °C) and an extensional relaxation time of 1.6 ms[15]. Moreover, the viscoelastic moduli showed a liquid-like behavior ($G'' > G'$) and gave evidence of the elastic character of the solution with a non-negligible storage modulus (see inset Fig. 3).

It must be noticed that reproducing the rheological behavior of blood is a very challenging issue[16]. These working fluids are considered blood analogues in the sense that they are able to reproduce the viscosity curve and the elastic character of the whole human blood as a bulk. On one hand, in the case of the Newtonian fluid, the similarity lies in the fact that it is able to reproduce the viscosity at high shear rates. The absent of elasticity makes this blood analogue useful for large vessels, where the elastic effects are negligible. On the other hand, the viscoelastic fluid is able to mimic the shear-thinning behavior and the elastic character of whole blood[15], making it more suitable for small vessels. In spite of the fact that none of them are able to capture other complex characteristic of the real blood, like the thixotropy[54] or the Fåhraeus-Lindqvist effect[55], they are considered as suitable blood analogues for microfluidic studies.[56].

The Reynolds number characterizing the flow in the microchannel is defined as $Re_c = \rho \cdot U_m \cdot 2L_c/\eta_\infty$, where ρ is the blood analogue fluid density, η_∞ is the constant viscosity and the plateau shear-viscosity at high shear-rates for the Newtonian and the viscoelastic fluids respectively, and U_m is the mean velocity in the microchannel. The flow rates Q considered ranged from 0.025 μl/s to 250 μl/s, leading to a Re_c interval from ∼0.01 up to ∼100 (characteristic of the flow regime in the human circulatory system at small-medium vessels[37]) for both the Newtonian and the viscoelastic blood analogue fluids. The mean velocities $U_m = Q/A_T$ in the microchannel were 48 μm/s $\leq U_m \leq$ 480 mm/s, being A_T the channel cross-section area. For the viscoelastic blood analogue, the characteristic Weissenberg number, Wi, is localy defined for the contraction on the microchannel cross-section created by the model at its center position ($X = 0$) as:

$$Wi = \lambda \cdot \dot{\gamma}\,; \qquad with \quad \dot{\gamma} = \frac{U_{contr}}{L_{contr}} \tag{1}$$

where λ is the extensional relaxation time of the viscoelastic blood analogue and $\dot{\gamma}$ the characteristic shear-rate in the contraction, being $U_{contr} \approx U_m \ \frac{L_c}{L_c - R_1}$ the averaged velocity at the cross-section $X = 0$ and $L_{contr} = R_1 \cdot \left(1 - \frac{R_1}{Lc}\right)$ the scaled length ratio for the "flow past a confined cylinder" problem[57]. The flow rate range tested in the experiments led to a shear-rate interval $1.28\ s^{-1} \leq \dot{\gamma} \leq\ 12800\ s^{-1}$ at the model cross-section and a local Weissenberg number ranging from 0.002 to 21 (see Fig 3). All the

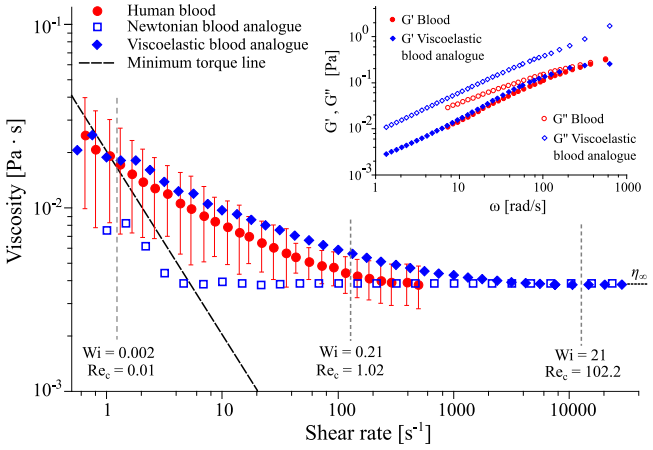

Fig. 3 Shear viscosity of the blood analogue fluids at 20 °C. Inset graph shows the lost and storage moduli for the viscoelastic blood analogue adapted from Campo-Deano et al.[15]. Data for human blood at 37 °C are also depicted, with error bars representing the standard deviation of the average values between F1 and M3 samples (see Valant et al.[58])

experiments were carried out at a controlled room temperature of 20 °C.

2.3 Experimental techniques

The flow rate was controlled by means of a neMESYS low pressure syringe pump (Cetoni GmbH). Depending on the flow rate, different glass syringes (Hamilton® 100 μl - 10 ml volume, and Fortuna® 20 ml volume) were used to ensure pulsation-free dosing. The pump controlled the inlet flow rate, while the outlet was left open to the atmosphere to balance the flow. Tygon® tubes with an inner diameter (i.d.) of 1.02 mm and precision dispensing tips 0.86 mm i.d. (Nordson Corporation) were used to connect the syringe output to the microdevice inlet hole through the 5 mm thickness PDMS block and, in the same way, the outlet hole to an atmospheric fluid reservoir.

The flow dynamics in the microchannel were characterized experimentally using μPIV following the procedure detailed by Oliveira et al.[59]. This is a well established technique for measuring spatially resolved velocity fields at small length scales associated with microfluidic devices[60,61]. The microchannel was placed on the imaging stage of an inverted microscope (Leica DMI 5000 M) equipped with 10x and 20x magnification objective lenses (Leica HCX PL-Floutar, numerical aperture NA = 0.30 and NA = 0.4, respectively). A CCD camera (Dantec Dynamics FlowSense EO-4M) 2048 x 2048 pixels connected to the microscope was used to acquire the images at the mid-plane ($Y = 0$), as well as at different planes below the mid-plane (0 μm $\leq Y \leq$ +70 μm). A double-pulsed 532 nm wavelength Nd:YAG laser system was used for volume illumination and 1 μm diameter fluorescent particles (FluoSphere®, carboxylate-modified nile red, Ex/Em = 535/575 nm) at a concentration of ∼20 ppm for the solids fraction were used as tracer particles. An epifluorescent filter cube was used to prevent the laser light from reaching the sensor of the CCD camera, which receives only the light emitted by the fluorescent particles.

The time lapse between two consecutive frames was adjusted

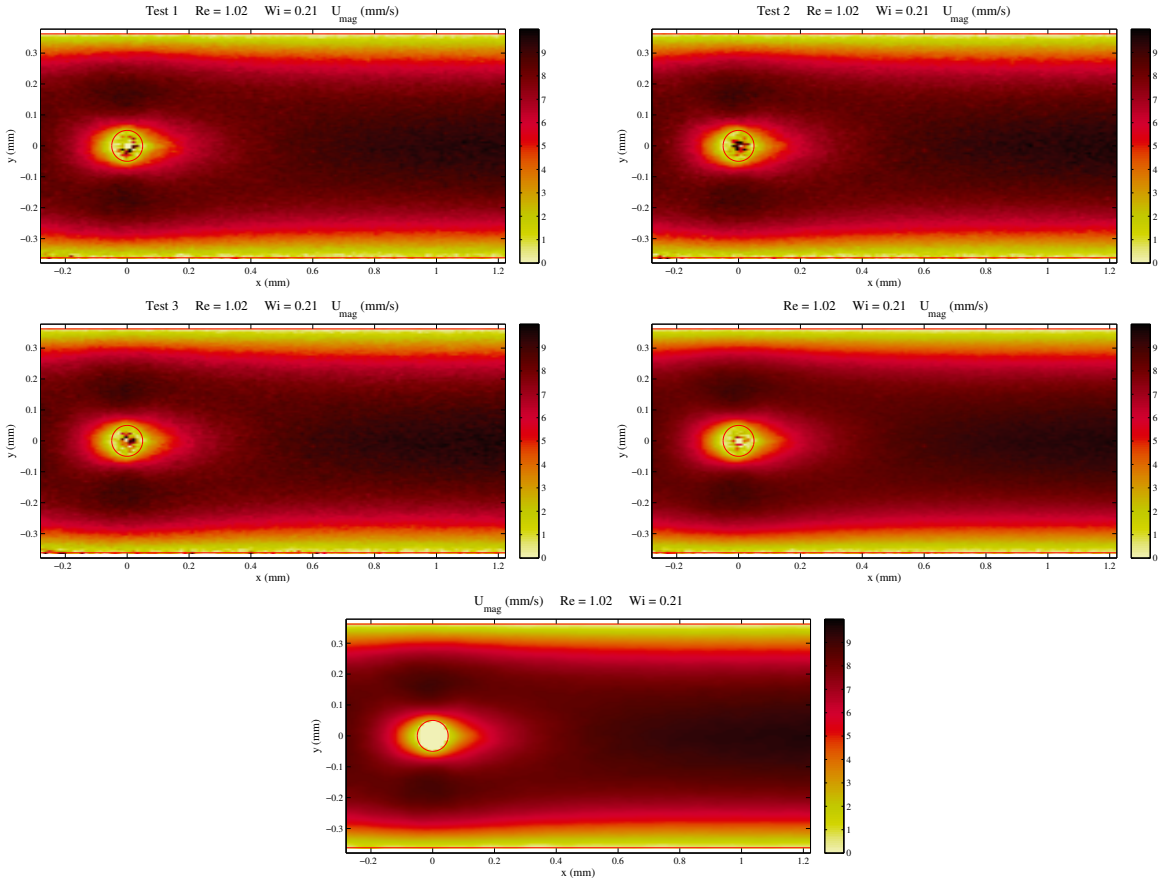

Fig. 4 Raw data from three independent measurements, their average (second row on the right) and their smoothed velocity field (third row) for the case of the sphere with the viscoelastic blood analogue at Re_c=1.

depending on the flow rate in order to ensure that the frame-by-frame particle displacement was optimal for subsequent analysis using an adaptive cross-correlation PIV algorithm with interrogation areas ranging from 16×32 pixels to 32×64 pixels, depending on the lens used. For each experiment, a minimum of 100 image pairs were recorded and processed to perform an averaged cross-correlation analysis using the *Dynamic Studio* software (version 2.30.47, Dantec Dynamics) in order to obtain the velocity field in the test section. The post-processing of these velocity data was performed by means of in-built Matlab® codes. Each test was repeated at least three times. Final velocity results for each case were averaged from the experimental data set for each flow condition and then slightly smoothed using a fast robust version of the method introduced by Garcia[62,63]. This method is based on the discrete cosine transform (DCT), allowing robust smoothing of equally spaced data in two dimensions by means of the penalized least squares approach. Figure 4 shows an example of raw data from three independent measurements, their average and their smoothed velocity field for the case of the sphere with the viscoelastic blood analogue at Re_c=1.

3 Experimental results and discussion

The first difference observed between the viscoelastic and Newtonian blood analogue flows was in the fully developed velocity profiles $u(z)$ at the mid-plane upstream of the model section (data not shown here). For low Reynolds numbers in the channel ($Re_c \leq 0.51$), the fully developed profile became more flattened as the flow rate increased, and the maximum streamwise velocity at center of the cross-stream section was significantly lower than that for the Newtonian case $U_{fdf} = max(u)/U_m \approx 2.0962$ in square cross-section microchannels[64], which is the typical velocity profile produced by the shear thinning behavior. The maximum deviation of the viscoelastic fully developed flow velocity at the center of the channel with respect to the Newtonian case was about 15% U_m, at $Re_c = 0.51$. As the Re_c increased further, the viscoelastic fully developed flow profile tends to agree with the Newtonian case, as the second Newtonian plateau in the viscosity curve, η_∞, was progressively reached and both fluids almost exhibit a similar constant viscosity (see Fig. 3). For $Re_c \geq 25.6$, the difference of the velocity in the centerline of the microchannel was lower than 1.5% U_m.

Fig. 5 and Fig. 6 depict the streamwise velocity u contours at the microchannel mid-plane ($Y = 0$) with both the Newtonian (dotted lines) and viscoelastic (solid lines) blood analogues. For $Re_c \leq 1.02$ velocity contours up and downstream of the models were practically symmetric for the Newtonian analogue fluid, confirming that the flow was at Stokes regime and inertial effects were negligible. As Re_c increased further than 1.02, inertial effects appeared and wakes became longer, losing symmetry with respect to the upstream velocity field. Generally, the larger

the flow rate in the channel, the longer the wake downstream became for all the models, which is the typical effect of inertia regardless of the fluid nature. Nevertheless, the viscoelastic blood analogue showed asymmetric velocity contours upstream and downstream of all the models even at low Re_c. The streamwise velocity contours behind the models for the viscoelastic flow were much sharper at the center of the channel than for the Newtonian case, especially at reduced flow rates. It is known that in the "viscoelastic flow past a confined cylinder" problem, the most remarkable elastic effect occurs at the wake behind the cylinder where the "stretching" of the fluid downstream of the rear stagnation point creates a high normal stress component[65–67]. These sharp shapes observed for the streamwise velocity u contours at the model wake with the viscoelastic blood analogue fluid seem to be in agreement with the region where the highest normal stresses are expected.

Furthermore, these sharp shapes also became more distinguishable as the flow rate in the channel increased, until the Re_c reached the value 10.2 (Wi = 2.1), at which the most marked peaks in the wake velocity contours were observed behind all the models. Then, as the Re_c increased further, the differences between Newtonian and viscoelastic velocities seem to reduce and contours practically agree at Re_c = 51.1 (Wi = 10). However, at the highest Reynolds number explored here (Re_c = 102.2; Wi = 21), differences on the velocity contours appeared again, except for the E2 model, which showed the maximum similarity between Newtonian and viscoelastic behavior at the highest Re_c, leading to think that this model undergoes lower normal stresses at its wake as the flow rate in the channel increases. Additionally, for the Newtonian blood analogue fluid, two steady symmetrical recirculation vortex caused by inertia appeared downstream of the CU model at $Re_c = 51.1$ (increasing in length as the Re_c increased) and the SP model at $Re_c = 102.2$, see Fig. 7 bottom part. The two ellipsoidal models did not show any kind of recirculation zone downstream with the Newtonian blood analogue, even at the highest Reynolds number. However, these vortex behind CU and SP models did not appear for the viscoelastic blood analogue fluid at any Re_c and the velocity streamlines always remained attached to the model rear surface (Fig. 7 top part). Song et al.[68] reported that shear-thinning effect on a Poiseuille flow past a confined sphere tends to increase the length of the inertial recirculation zones behind the model with respect to the Newtonian case. Therefore, the suppression of these inertial vortex downstream of the CU and SP models for the viscoelastic blood analogue may be directly related to the fluid elasticity[69], which is enhanced by the micro-scale dimensions of the immersed body.

Focusing the analysis on the velocity evolution at the channel centerline downstream of the model rear stagnation point, generally the viscoelastic blood analogue flow also presented longer wakes in comparison to the Newtonian case and the axial velocity u profiles were shifted downstream for the viscoelastic blood analogue, especially at low Re_c (Fig. 8[a]). The normalized streamwise velocity difference between viscoelastic and Newtonian cases along the wake centerline, Δu, was defined as $\Delta u = \frac{u_{visc} - u_{Newt}}{U_m}$, where u_{visc} and u_{Newt} are the streamwise velocities for the viscoelastic and Newtonian blood analogue fluids,

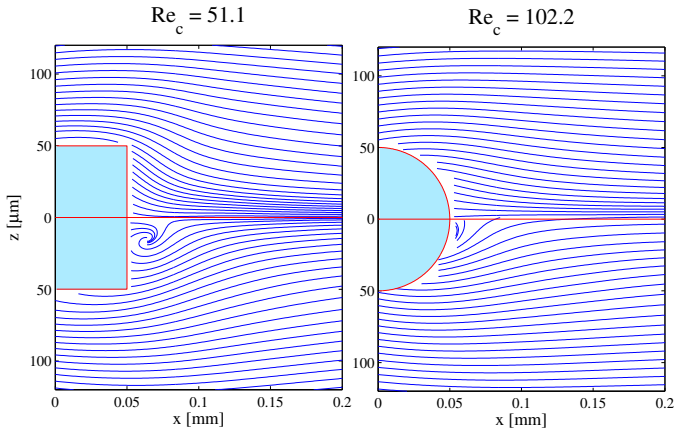

Fig. 7 Velocity streamlines at the plane $Y = 0$, computed from experimental μPIV data for Newtonian (bottom part) and viscoelastic (top part) blood analogue fluid flows around the cube and sphere models.

respectively, at the same point. Fig. 8[b] depicts the Δu profiles for the CU model, showing the other models a similar behavior. In general for all the prototypes, Δu profiles at the rear wake centerline showed a positive zone (higher velocities for the viscoelastic fluid than for the Newtonian case) near to the model surface ($x_w < 4 \cdot R_1$) and then a marked negative Δu zone (lower velocities for the viscoelastic fluid than for the Newtonian case) farther away from the rear stagnation point. We defined Δu_{max} as the maximum value of the positive normalized velocity difference zone and Δu_{min} as the minimum of the negative zone. Inset in Fig. 8[b] shows the values of Δu_{max} (open symbols) and Δu_{min} (closed symbols) for all the models as a function of the local Wi at the model contraction.

At low Reynolds numbers ($Re_c \leq 1.02$ and $Wi \leq 0.21$), the negative zone of Δu was much more marked than the positive one, leading to shift downstream the axial velocity patterns, as it was mentioned previously. At these low inertia regimes, the positive zone even disappeared for most of the cases and Δu_{min} and Δu_{max} values did not present clear tendencies. However, Δu behavior appears to have a critical threshold for Wi = 1.0 (Fig. 8[b]). For $Wi \geq 1.0$ ($Re_c \geq 5.11$), a clear tendency appears in both negative and positive Δu zones. The negative zone begins to decrease progressively and its minimum Δu_{min} became less marked and it was reached farther away to the model rear stagnation. For the two highest Reynolds number in the channel ($Re_c = 51.1$ and 102.2), the negative Δu zone almost disappeared. Furthermore, the positive zone near to the model rear stagnation point was clearly more distinguishable at high flow rates, increasing its length and its maximum value Δu_{max} monotonously as the Wi increases.

Zheng et al.[70] studied separately inertia, shear-thinning and elasticity effects on a sphere immersed in a cylindrical Poiseuille flow. On one hand, they reported that when inertia effects are negligible, the modification of the axial velocity field behind the sphere due to the shear-thinning effects is mainly found in the region near the rear stagnation points and it consists of shifting the velocity profile toward the sphere surface, i.e. $\Delta u > 0$. On the other hand, Zheng et al.[70] also reported that elasticity effects

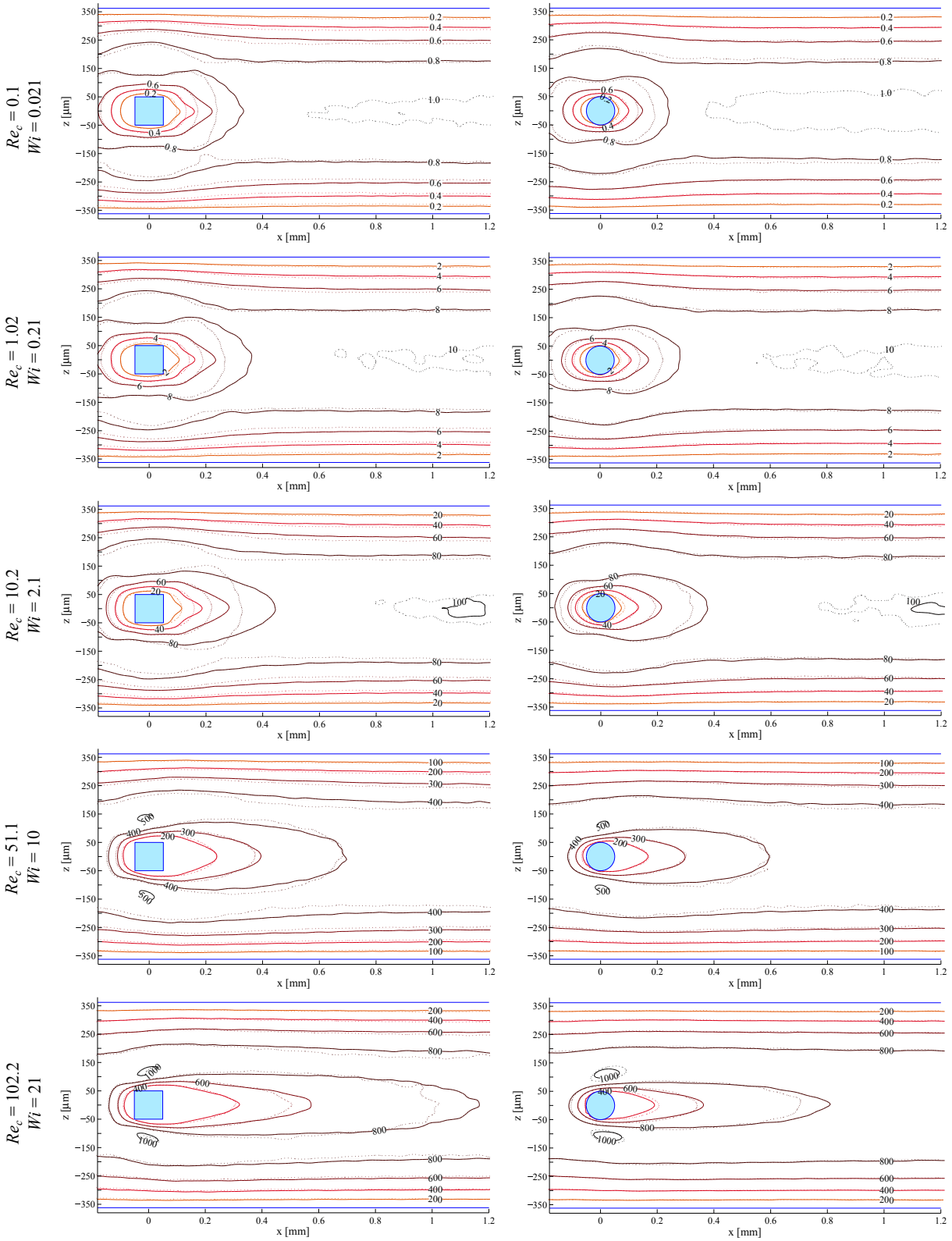

Fig. 5 Experimental Newtonian (dotted lines) and viscoelastic (solid lines) streamwise velocity u contours [mm/s] at the measurement plane $Y = 0$ for the CU and SP models at different Re_c and Wi.

tend to decrease the acceleration of the fluid behind the sphere, i.e. $\Delta u < 0$, and thus to translate the flow patterns in the downstream direction even if inertial effects are presented. Therefore, these observed negative Δu zones dominating the wake centerline profile at low Re_c may be mainly caused by the elasticity of the blood analogue more than by the shear-thinning effects. Al-

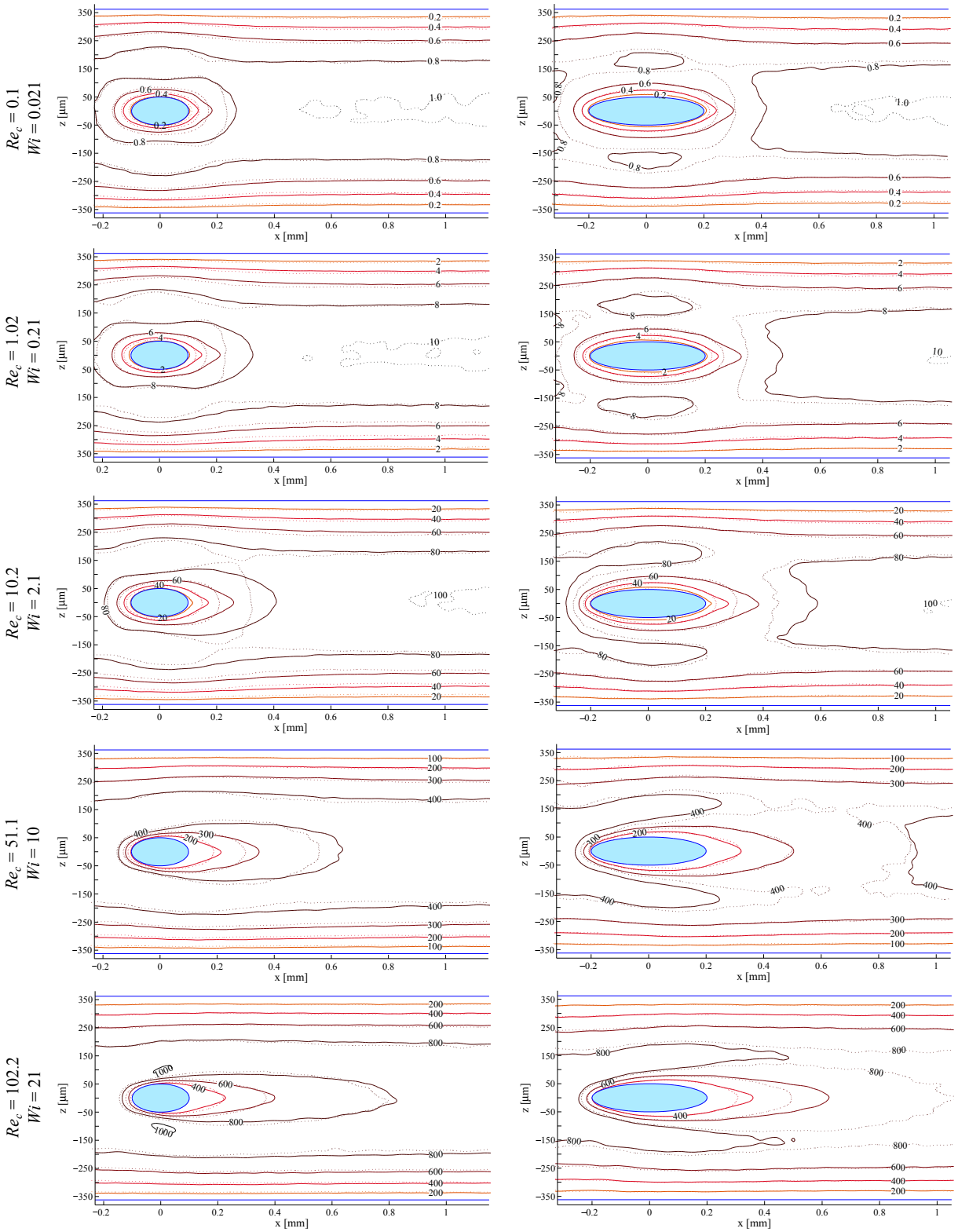

Fig. 6 Experimental Newtonian (dotted lines) and viscoelastic (solid lines) streamwise velocity u contours [mm/s] at the measurement plane $Y = 0$ for the E2 and E4 models at different Re_c and Wi.

though the fluid elasticity was almost insignificant considering macro-scale conditions, the micro-scale characteristic length of the model caused an enhancement of the elasticity effects undergone by the fluid. As the flow rate increased ($Re_c \geq 5.11$ and $Wi \geq 1.0$), inertial effects begin to dominate the flow over shear-thinning and elasticity effects, hence Newtonian and viscoelastic velocity contours appeared to approach, although some differences associated to shear-thinning effects remain in the region

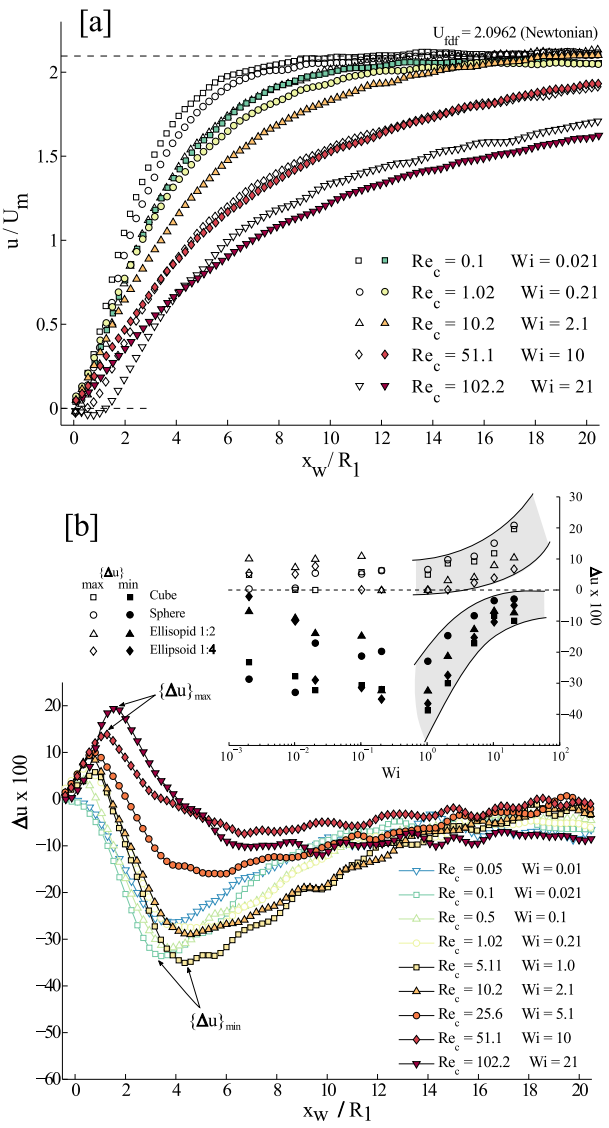

Fig. 8 [a] Normalized streamwise velocity at the rear wake centerline of the CU model for Newtonian (open symbols) and viscoelastic (closed symbols) blood analogue fluids. [b] Normalized streamwise velocity difference Δu at the rear wake centerline for the CU model, expressed as percentage of the mean velocity in the microchannel (U_m). Inset depicts maximum and minimum of the positive and negative Δu zones, respectively, as a function of the local Wi at the model section.

near to the rear stagnation point ($\Delta u \geq 0$).

Comparison between the streamwise velocity u of the viscoelastic blood analogue, normalized by the mean velocity in the channel U_m, at the rear wake (Fig. 9) shows clear differences between the models. CU model created the most marked wake near to the model rear stagnation point, regardless of the flow rate in the channel. The streamwise velocity u at the channel centerline behind the E2 model recovers the fully developed flow value faster than the other models, even than the more slender E4 ellipsoid. The spherical prototype showed a velocity profile intermediate between the CU and the E2 models, and even it appeared to recover the fully developed profile faster than the E4 model at the end of the wake. At low Reynolds numbers in the channel ($Re_c \leq 0.51$) the flow at the plane $Y = 0$ practically has recover the fully developed profile at $x_w = 10 \cdot R_1 = 500\,\mu$m from the rear stagnation point. For $1.02 \leq Re_c \leq 10.2$ the profile at the center-plane remained slightly altered at $x_w = 500\,\mu$m, but it almost agreed with the fully developed profile at $x_w = 16 \cdot R_1 = 800\,\mu$m downstream of the model. For $Re_c > 10.2$ streamwise velocity did not recover the fully develop profile even at $x_w = 800\,\mu$m ($16 \cdot R_1$). Ellipsoid 1:2 model presented the shortest wake regardless of the mean flow velocity, although as Re_c increased the velocity profile was progressively approaching to that of the SP model.

In order to establish a quantitative comparison of the model efficiency in terms of flow disturbance, the control-volume approach was used applied to the velocity measurements at the channel mid-plane. The control-volume method allows the integral load on an object to be obtained from an integration of the flow variables inside a control volume surrounding this object[71]. This non-intrusive method has been extensively used to obtain aerodynamic forces on 2D airfoil profiles immersed in turbulent unbounded air flows, as occurs in wind tunnels, from PIV data[72–74]. Required flow field properties needed to apply this method are velocity, pressure and viscous stresses on the outer contour s of a control volume V enclosing the considered body. In the Newtonian and unbounded case, these properties can be evaluated from the instantaneous or time-averaged velocity field obtained by PIV technique. Here, a new approach is proposed to analyze the global disturbance in the channel flow caused by the presence of the microbot in the center of the cross-section. Considering a fixed 2D control-volume in the measurement plane $Y = 0$, which contains our microbot prototype and enclosing the whole microchannel width, and two-dimensional steady flow, the time-mean momentum conservation equation in this control volume can be expressed in its integral form as:

$$\int_s \rho \mathbf{u}\,\mathbf{u}\cdot\hat{\mathbf{n}}\,\mathrm{d}s = \int_s (-p\hat{\mathbf{n}} + \boldsymbol{\tau}\cdot\hat{\mathbf{n}})\,\mathrm{d}s - \mathbf{F} \qquad (2)$$

where ρ, p, $\mathbf{u}$, τ and $\hat{\mathbf{n}}$ are the fluid density, the pressure value, the 2D velocity vector, the stress tensor and the outward pointing normal vector, respectively, on each point of the outer contour s, and $\mathbf{F}$ is 2D integral force experienced by the model in its mid-plane. The cross-stream direction component of the vector equation system (Eq. 2) can be unattended since it will be always balanced due to the flow symmetry with respect to the Y-plane longitudinal centerline.

The left hand in Eq. 2 quantifies the integral momentum deficit for the control-volume and it is unambiguous related to the velocity field, therefore it can be directly evaluated from μPIV data. The first term of the right hand in Eq. 2 represents the integral balance between pressure drop along the channel and the stresses on the channel walls. For a clean section of the channel, i.e. without model ($\mathbf{F} = 0$), pressure drop and X-direction stress component on the channel walls are balanced and hence the momentum deficit is null, resulting in the fully developed flow regime. However, the presence of the model leads to an non-null integral momentum deficit for the successive length-increasing control-volumes along the wake of the microbot, considering that all these control-volumes start at the same fixed section with fully developed flow profile upward the model. As the control-volume

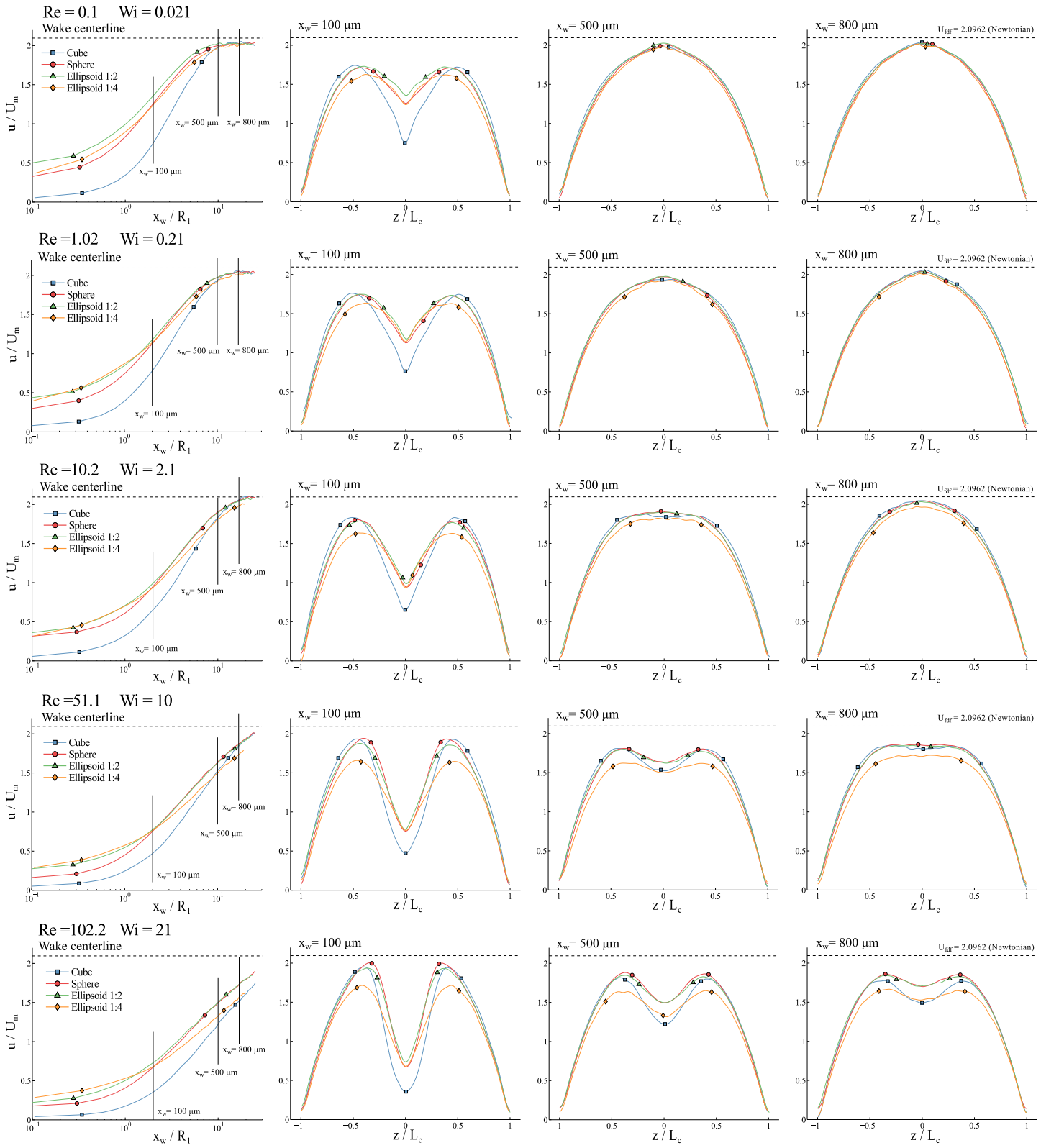

Fig. 9 Normalized streamwise velocity u/U_m profiles at the channel mid-plane for all the models and the viscoelastic blood analogue fluid. First column: streamwise channel centerline at the rear wake. Second-Forth columns: cross-stream direction lines at different positions (x_w) downstream of the rear stagnation point.

exit moves far away from the rear stagnation point, the integral momentum deficit decreases until it becomes null (wake end) and the right hand terms of Eq. 2 are balanced once again (see scheme in Fig. 10[a]). The integration along the wake of the integral momentum deficit value allows us to propose a quantitative characterization parameter $\Im$ of the energy dissipated by the flow to

fully pass the microbot prototype, as defined in Eq. 3:

$$\Im = \int_{X_{w_{end}}} \left(\int_{S_k} \rho \mathbf{u}\,\mathbf{u} \cdot \hat{\mathbf{n}} \mathrm{d}s \right) \mathrm{d}x_w \tag{3}$$

$\Im$ represents a global criterion to compare the efficiency of the models in terms of flow disturbance ($\Im$ has units of joules/meter). The marker and longer the wakes are, the higher $\Im$ becomes, what means that a greater disturbance in the channel flow has been caused by the model.

Therefore, we computed the X-component of the integral momentum deficit from the measured μPIV fields at the channel mid-plane. All the 2D control-volumes started at a fully developed flow section upward the model. The ending section moved successively from the rear stagnation point to a section downstream of the model at which the streamwise velocity u at the channel centerline had recovered a 80% of the fully developed flow value for each case. Then this integral momentum deficit was numerically integrated along the X-direction in order to obtain the efficiency parameter $\Im$. The momentum in the channel flow increases in the same order of magnitude than u^2 grows, hence in order to improve the visualization of the results through the whole velocity range tested, values of $\Im$ have been scaled by Re_c^2 and shown in Fig. 10.

Firstly, comparison of models for the viscoelastic blood analogue fluid (Fig. 10[b]) indicates that the CU model presents the worst dynamic efficiency (in terms of the flow disturbance) at low Reynolds numbers in the channel, as it was expected. Furthermore, the SP and E2 models show again a quite similar behavior, especially at high Re_c, but the E2 model develops slightly lower values of $\Im$. For these three models, a change in the tendencies appears at $Re_c \approx 0.51$ ($Wi \approx 0.1$), coinciding with the critical Re_c for the shear-thinning effects on the fully developed flow profile in the channel. The larger ellipsoidal model E4 suffers a quick deterioration of its efficiency as the Re_c increases, probably caused by its much higher surface which may lead to the enhancement of the stresses in the near region of the viscoelastic fluid. Even at $Re_c \geq 5.11$ ($Wi \geq 1.0$), the E4 model shows worse $\Im$ values than the CU model. Therefore, it seems that the E2 model shows again the best efficiency for viscoelastic blood analogue, regardless of the flow rate in the channel. Regarding to the Newtonian blood analogue (inset in Fig. 10[b]), all the rounded models, i.e. SP, E2 and E4, showed very closed $\Im$ values at low flow rates in the microchannel. The result for the SP model shows a good agreement with the numerical prediction for the untethered model (open circles). The CU model showed much higher $\Im$ values than all the other models, indicating it was the worst model in terms of channel flow alteration, at reduced flow rates in the channel. At higher flow rates, the $\Im$ value for the E4 model increases as in the case of the viscoelastic flow, even reaching the values for the CU model. Finally, the critical threshold for the $\Im/Re_c^2$ tendency observed for the viscoelastic blood analogue at $Re_c = 0.51$ seems to disappear, confirming that it may be related to the non-Newtonian behavior of the fluid.

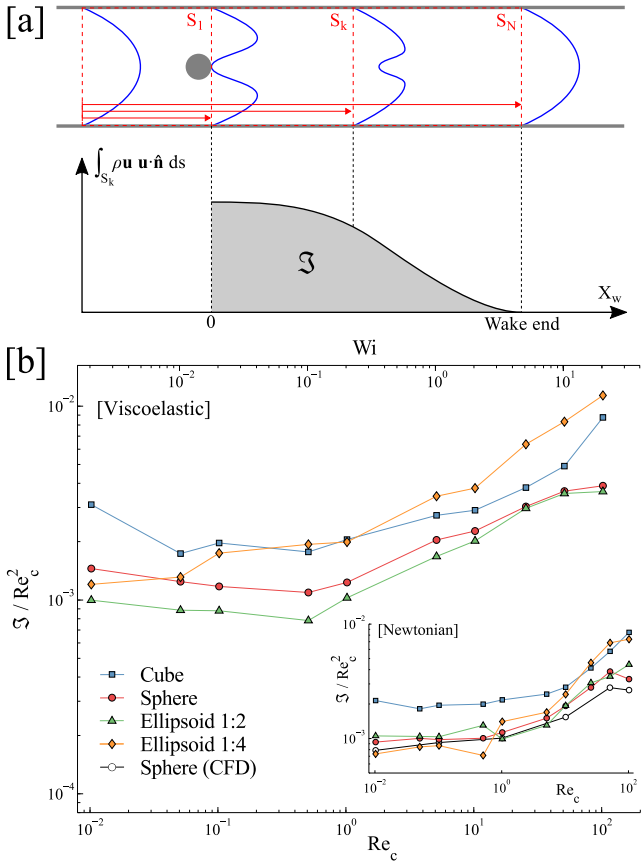

Fig. 10 Efficiency parameter $\Im$: [a] Sketch for the $\Im$ calculation; [b] Results ($\Im$ scaled by Re_c^2) for the viscoelastic blood analogue fluid. The inset in [b] depicts the results for the Newtonian case together with the numerical prediction for the untethered SP model evaluated from the CFD simulations.

4 Conclusions

A new micro-hydrotunnel for the study of the complex fluid flow dynamics around 3D microbot prototypes has been successfully designed, implemented and validated. μPIV measurements and the proposed efficiency parameter $\Im$, which represents a value of the energy dissipated in the flow by the presence of the microbot in the center of the channel, allowed us to clearly discriminate the prototypes in terms of the flow disturbance.

Results showed that, even when the elasticity of the blood analogue fluid is very low ($\lambda = 1.6$ ms), its influence in the fluid velocity field around the microbot is clearly marked, especially at non-inertia conditions. With regards to the model performance, the best efficiency corresponds to the ellipsoid 1:2 in both blood analogue flows, Newtonian and viscoelastic. On the contrary, the cube model presented a larger disturbance of the flow, especially when inertia effects are negligible (low flow rates). The particular case of the ellipsoid 1:4 must be highlighted due to its unsatisfactory efficiency at high Re_c. Probably, this performance deterioration for the E4 model may be associated to its much higher surface in comparison to the spherical or the shorter ellipsoidal models.

This study provides a useful tool for selecting the best microbot's morphology depending on its foreseen application, as the

Re_c varies from a medium size artery to capillaries. For example, for a removing clots application, the cubic or larger ellipsoidal shapes could be the best choice hence they create a higher disturbance on the flow conditions and, thus, may dissolve the clot easily. On the contrary, for drug delivery close to sensitive zones of the circulatory system (as could be an aneurysm), spherical or shorter ellipsoidal shapes would help to reduce risks since the disturbance induced in the vessel flow will be limited.

In future works it is expected to obtain the drag forces exerted on the prototypes. This is a non-trivial measurement as the shear stresses originated by the viscoelastic fluid are difficult to obtain. These study will be performed by means of birefringence techniques which are able to generate a contour map of stresses.

Acknowledgments

Authors would like to acknowledge financial support from FCT, COMPETE and FEDER through projects EXPL/EMS-TRA/2306/2013 and PTDC/EQU-FTT/118716/2010 and grants IF/00148/2013 and IF/00190/2013.

References

1 B. J. Nelson, I. K. Kaliakatsos, J. J. Abbott, Microrobots for minimally invasive medicine, Annual Review of Biomedical Engineering 12 (2010) 55–85. Doi:10.1146/annurev-bioeng-010510-103409.

2 A. Ghanbari, M. Bahrami, A novel swimming microrobot based on artificial cilia for biomedical applications, J. Intell. Robot. Syst. 63 (2011) 399–416. Doi:10.1007/s10846-010-9516-6.

3 M. Takeda, Applications of mems to industrial inspection, in: IEEE International Conference on Micro-Electro-Mechanical Systems (MEMS), pp. 182–191. Doi:10.1109/MEMSYS.2001.906510.

4 S. Martel, Magnetic microbots to fight cancer, IEEE Spectrum (2012). Http://spectrum.ieee.org/robotics/medical-robots/magnetic-microbots-to-fight-cancer.

5 W. Zhu, J. Li, Y. J. Leong, I. Rozen, X. Qu, R. Dong, Z. Wu, W. Gao, P. H. Chung, J. Wang, S. Chen, 3D-printed artificial microfish, Advanced Materials 27 (2015) 4411–4417.

6 O. Ergeneman, G. Chatzipirpiridis, J. Pokki, M. Marin-Suarez, G. A. Sotiriou, S. Medina-Rodriguez, J. F. Sanchez, A. Fernandez-Gutierrez, S. Pane, B. J. Nelson, In vitro oxygen sensing using intraocular microrobots, IEEE Trans Biomed Eng 59 (2012) 3104–3109. Doi:10.1109/TBME.2012.2216264.

7 M. Sitti, Miniature devices: voyage of the microrobots, Nature 458 (2009) 1121–1122. Doi:10.1038/4581121a.

8 R. J. Poole, The Deborah and Weissenberg numbers, Rheology Bulletin 53 (2012) 32–39.

9 F. J. Galindo-Rosales, L. Campo-Deaño, P. C. Sousa, V. M. Ribeiro, M. S. N. Oliveira, M. M. Alves, F. T. Pinho, Viscoelastic instabilities in micro-scale flows, Experimental Thermal and Fluid Science 59 (2014) 128–139. Doi:10.1016/j.expthermflusci.2014.03.004.

10 G. B. Thurston, Rheological parameters for the viscosity, viscoelasticity and thixotropy of blood, Biorheology 16 (1979) 149–162.

11 L. Dintenfass, Blood rheology in cardio-vascular diseases, Nature 199 (1963) 813–815.

12 L. Langstroth, Blood viscosity. I Conditions affecting the viscosity of blood after withdrawal from the body, The Journal of Experimental Medicine 30 (1919) 597–606.

13 S. Chien, S. Usami, R. J. Dellenback, M. I. Gregersen, Blood viscosity: influence of erythrocyte deformation, Science 157 (1967) 827–829.

14 S. Chien, S. Usami, R. J. Dellenback, M. I. Gregersen, L. B. Nanninga, M. M. Guest, Blood viscosity: influence of erythrocyte aggregation, Science 157 (1967) 829–831.

15 L. Campo-Deaño, R. P. A. Dullens, D. G. A. L. Aarts, F. T. Pinho, M. S. N. Oliveira, Viscoelasticity of blood and viscoelastic blood analogues for use in polydymethylsiloxane in vitro models of the circulatory system, Biomicrofluidics 7 (2013) 034102. Doi:10.1063/1.4804649.

16 L. Campo-Deaño, M. S. N. Oliveira, F. T. Pinho, A review of computational hemodynamics in middle cerebral aneurysms and rheological models for blood flow, Applied Mechanics Reviews 67 (2015) 030801. Doi:10.1115/1.4028946.

17 A. J. Apostolidis, M. J. Armstrong, A. N. Beris, Modeling of human blood rheology in transient shear flows, Journal of Rheology 59 (2015).

18 A. J. Apostolidis, A. N. Beris, Modeling of the blood rheology in steady-state shear flows, Journal of Rheology 58 (2014).

19 M. Brust, C. Schaefer, R. Doerr, L. Pan, M. Garcia, P. E. Arratia, C. Wagner, Rheology of human blood plasma: Viscoelastic versus newtonian behavior, Physical Review Letters 110 (2013) 078305. Doi:10.1103/PhysRevLett.110.078305.

20 T. Qiu, T.-C. Lee, A. G. Mark, K. I. Morozov, R. Münster, O. Mierka, S. Turek, A. M. Leshansky, P. Fischer, Swimming by reciprocal motion at low Reynolds number, Nature Communications 5 (2014) 5119. Doi:10.1038/ncomms6119.

21 B. Qin, A. Gopinath, J. Yang, J. P. Gollub, P. E. Arratia, Flagellar kinematics and swimming of algal cells in viscoelastic fluids, Scientific Reports 5 (2015) 9190. Doi:10.1038/srep09190.

22 M. A. Zeeshan, R. Grisch, E. Pellicer, K. M. Sivaraman, K. E. Peyer, J. Sort, B. Ozkale, M. S. Sakar, B. J. Nelson, S. Pané, Hybrid helical magnetic microrobots obtained by 3D template-assisted electrodeposition, Small 10 (2014) 1284–1288. Doi10.1002/smll.201302856.

23 S. Kim, F. Qiu, S. Kim, A. Ghanbari, C. Moon, L. Zhang, B. J. Nelson, H. Choi, Fabrication and characterization of magnetic microrobots for three-dimensional cell culture and targeted transportation, Advanced Materials 25 (2013) 5863–5868. Doi:10.1002/adma.201301484.

24 M. Suter, L. Zhang, E. C. Siringil, C. Peters, T. Luehmann, O. Ergeneman, K. E. Peyer, B. J. Nelson, C. Hierold, Superparamagnetic microrobots: fabrication by two-photon polymerization and biocompatibility, Biomedical Microdevices 15 (2013) 997–1003.

25 T. W. R. Fountain, P. V. Kailat, J. J. Abbott, Wireless control of magnetic helical microrobots using a rotating-permanent-magnet manipulator, in: IEEE International Conference on Robotics and Automation. Anchorage, USA.

26 A. A. Solovev, S. Sanchez, M. Pumera, Y. F. Mei, O. G. Schmidt, Magnetic control of tubular catalytic microbots for the transport, assembly, and delivery of micro-objects, Advanced Functional Materials 20 (2010) 2430–2435.

27 J. J. Abbott, K. E. Peyer, L. X. Dong, B. J. Nelson, How should microrobots swim?, Springer Tracts in Advanced Robotics 66 (2011) 157–167.

28 K. Belharet, D. Folio, A. Ferreira, Three-dimensional controlled motion of a microrobot using magnetic gradients, Advanced Robotics 25 (2011) 1069–1083.

29 A. Palagi, E. W. H. Jager, B. Mazzolai, L. Beccai, Propulsion of swimming microrobots inspired by metachronal waves in ciliates: from biology to material specifications, Bioinspiration and Biomimetics 8 (2013) 046004.

30 K. E. Peyer, L. Zhang, B. J. Nelson, Bio-inspired magnetic swimming microrobots for biomedical applications, Nanoscale 5 (2013) 1259–1272. Doi:10.1039/C2NR32554C.

31 K. E. Peyer, E. C. Siringil, L. Zhang, M. Suter, B. J. Nelson, Bacteria-inspired magnetic polymer composite microrobots, Lecture Notes in Computer Science 8064 (2013) 216–227.

32 B. U. Felderhof, Self-propulsion of a planar electric or magnetic microbot immersed in a polar viscous fluid, Phys. Rev. E 83 (2011) 056315. Doi:10.1103/PhysRevE.83.056315.

33 I. S. M. Khalil, H. C. Dijkslag, L. Abelmann, S. Misra, Magnetosperm: A microrobot that navigates using weak magnetic fields, Applied Physics Letters 104 (2014) 223701. Doi:10.1063/1.4880035.

34 A. Sharafi, N. Olamaei, S. Martel, A new communication method for untethered intelligent microrobots, in: IEEE/ASME International Conference on Advanced Intelligent Mechatronics (AIM). Wollongong, Australia.

35 P. Corradi, O. Scholz, T. Knoll, A. Menciassi, P. Dario, An optical system for communication and sensing in millimeter-sized swarming microrobots, Journal of Micromechanics and Microengineering 19 (2009) 015022.

36 N. Boillot, D. Dhoutaut, J. Bourgeois, Using nano-wireless communications in micro-robots applications, in: ACM International Conference on Nanoscale Computing and Communication (NANOCOM). Atlanta, USA.

37 S. A. Berger, W. Goldsmith, E. R. Lewis, Introduction to Bioengineering, Oxford Univ. Press, Oxford, UK, 1996.

38 J. Black, G. Hastings, Handbook of Biomaterial Properties, Chapman & Hall, London, UK, 1998.

39 C. Pawashe, S. Floyd, M. Sitti, Modeling and experimental characterization of an untethered magnetic microrobot, Intern. J. Robotics Research 28 (2009) 1077–1094. Doi:10.1177/0278364909341413.

40 E. Diller, S. Floyd, C. Pawashe, M. Sitti, Control of multiple heterogeneous magnetic microrobots in two dimensions on nonspecialized surfaces, IEEE Transactions on Robotics 28 (2012) 172–182. Doi:10.1109/TRO.2011.2170330.

41 M. P. Kummer, J. J. Abbott, B. E. Kratochvil, R. Borer, A. Sengul, B. J. Nelson, OctoMag: An electromagnetic system for 5-DoF wireless micromanipulation, IEEE Transactions on Robotics 26 (2010) 1006–1017. Doi:10.1109/TRO.2010.2073030.

42 J. D. Keuning, J. de Vries, L. Abelmann, S. Misra, Image-based magnetic control of paramagnetic microparticles in water, in: IEEE/RSJ International Conference on Intelligent Robots and Systems (IROS), pp. 421–426. Doi:10.1109/IROS.2011.6095011.

43 I. S. M. Khalil, J. D. Keuning, L. Abelmann, S. Misra, Wireless magnetic-based control of paramagnetic microparticles, in: IEEE/RAS-EMBS International Conference on Biomedical Robotics and Biomechatronics (BioRob), pp. 460–466. Doi:10.1109/BioRob.2012.6290856.

44 I. A. Ivan, G. Hwang, J. Agnus, M. Rakotondrabe, N. Chaillet, S. Régnier, First experiments on MagPieR: A planar wireless magnetic and piezoelectric microrobot, in: IEEE International Conference on Robotics and Automation (ICRA), pp. 102 – 108. Doi:10.1109/ICRA.2011.5979885.

45 K. Belharet, D. Folio, A. Ferreira, Control of a magnetic microrobot navigating in microfluidic arterial bifurcations through pulsatile and viscous flow, in: IEEE/RSJ International Conference on Intelligent Robots and Systems (IROS). Doi:10.1109/IROS.2012.6386030.

46 I. S. M. Khalil, V. Magdanz, S. Sanchez, O. G. Schmidt, S. Misra, The control of self-propelled microjets inside a microchannel with time-varying flow rates, IEEE Transactions on Robotics 30 (2013) 49–58. Doi:10.1109/TRO.2013.2281557.

47 F. Z. Temel, S. Yesilyurt, Magnetically actuated micro swimming of bio-inspired robots in mini channels, in: IEEE International Conference on Mechatronics (ICM), pp. 342–347. Doi:10.1109/ICMECH.2011.5971307.

48 F. Z. Temel, S. Yesilyurt, Confined swimming of bio-inspired microrobots in rectangular channels, Bioinspiration and Biomimetics 10 (2015) 016015. Doi:10.1088/1748-3190/10/1/016015.

49 P. Y. Huang, J. Feng, Wall effects on the flow of viscoelastic fluids around a circular cylinder, J. Non-Newtonian Fluid Mech (1995).

50 S. Krishnan, A. Kaman, Effect of blockage ratio on drag and heat transfer from a centrally located sphere in pipe flow, Eng. Appl. Computational Fluid Mech. 4 (2010) 396–414. Doi:10.1080/19942060.2010.11015327.

51 J. B. Barlow, W. H. Rae, A. Pope, Low-Speed Wind Tunnel Testing, John Wiley & Sons, New York, USA, 1984.

52 R. G. Lebel, D. A. I. Goring, Density, viscosity, refractive index, and hygroscopicity of mixtures of water and dimethyl sulfoxide, J. Chem. Eng. Data 7 (1962) 100–101. Doi:10.1021/je60012a032.

53 U. R. Kapadi, S. K. Chavan, O. S. Yemul, Partial molar volumes and viscosity b coefficients of benzyltriethylammonium chloride in dimethyl sulfoxide + water at different temperatures, J. Chem. Eng. Data 42 (1997) 548–550.

Doi:10.1021/je960216+.

54 J. Vent-Schmidt, X. Waltz, M. Romana, M.-D. Hardy-Dessources, N. Lemonne, M. Billaud, M. Etienne-Julan, P. Connes, Blood thixotropy in patients with sickle cell anaemia: Role of haematocrit and red blood cell rheological properties, PLoS ONE 9 (2014) e114412.

55 R. Fåhraeus, T. Lindqvist, The viscosity of the blood in narrow capillary tubes, Am. J. Physiol. 96 (1931) 562–568.

56 C. C., G. V., S. V., Rheological and dynamical characterization of blood analogue flows in a slit, International Journal of Heat and Fluid Flow 46 (2014) 17–28. Cited By 2.

57 H. S. Dou, N. Phan-Thien, An instability criterion for viscoelastic flow past a confined cylinder, Korea and Australia Rheology Journal 20 (2008) 15–26.

58 A. Z. Valant, L. Ziberna, Y. Papaharilaou, A. Anayiotos, G. C. Georgiou, The influence of temperature on rheological properties of blood mixtures with different volume expanders - implications in numerical arterial hemodynamics simulations, Rheologica Acta (2011). Doi:10.1007/s00397-010-0518-x.

59 M. S. N. Oliveira, M. A. Alves, F. T. Pinho, G. H. McKinley, Viscous flow through microfabricated hyperbolic contractions, Experiments in fluids 43 (2007) 437–451.

60 J. G. Santiago, S. T. Wereley, C. D. Meinhart, D. J. Beebe, R. J. Adrian, A particle image velocimetry system for microfluidics, Experiments in Fluids 25 (1998) 316–319.

61 C. D. Meinhart, S. T. Wereley, M. H. B. Gray, Volume illumination for two-dimensional particle image velocimetry, Measurement Science and Technology 11 (2000) 809.

62 D. Garcia, Robust smoothing of gridded data in one and higher dimensions with missing values, Computational Statistics and Data Analysis 54 (2010) 1167–1178. Doi:10.1016/j.csda.2009.09.020.

63 D. Garcia, A fast all-in-one method for automated post-processing of PIV data, Experiments in Fluids 50 (2011) 1247–1259. Doi:10.1007/s00348-010-0985-y.

64 K. V. Sharp, R. J. Adrian, J. G. Santiago, J. I. Molho, MEMS: Introduction and Fundamentals, Taylor & Francis Group, Boca Raton, USA.

65 M. A. Alves, F. T. Pinho, P. J. Oliveira, The flow of viscoelastic fluids past a cylinder: finite-volume high-resolution methods, J. Non-Newtonian Fluid Mechanics 97 (2001) 207–232. Doi:10.1016/S0377-0257(00)00198-1.

66 P. J. Oliveira, A. I. Miranda, A numerical study of steady and unsteady viscoelastic flow past bounded cylinders, J. Non-Newtonian Fluid Mech. 127 (2005) 51–66. Doi:10.1016/j.jnnfm.2005.02.003.

67 A. Afonso, M. A. Alves, F. T. Pinho, P. J. Oliveira, Uniform flow of viscoelastic fluids past a confined falling cylinder, Rheologica Acta 47 (2008) 325–348. Doi:10.1007/s00397-007-0234-3.

68 D. Song, R. K. Gupta, R. P. Chhabra, Drag on a sphere in poiseuille flow of shear-thinning power-law fluids, Ind. Eng. Chem. Res. 50 (2011) 13105–13115. Doi:10.1021/ie102120p.

69 L. E. Rodd, T. P. Scott, D. V. Boger, J. J. Cooper-White, G. H. McKinley, The inertio-elastic planar entry flow of low-viscosity elastic fluids in micro-fabricated geometries, J. Non-Newtonian Fluid Mech. 129 (2005) 1–22.

70 R. Zheng, N. Phan-Thien, R. I. Tanner, The flow past a sphere in a cylindrical tube: effects of inertia, shear-thinning and elasticity, Rheologica Acta 30 (1991) 499–510. Doi:10.1007/BF00444368.

71 J. D. Anderson, Fundamentals of Aerodynamics, McGraw-Hill, New York, USA, 1991.

72 B. W. van Oudheusden, F. Scarano, E. W. F. Casimiri, Non-intrusive load characterization of an airfoil using PIV, Experiments in Fluids 40 (2006) 988–992. Doi:10.1007/s00348-006-0149-2.

73 D. Ragni, A. Ashok, B. W. van Oudheusden, F. Scarano, Surface pressure and aerodynamic loads determination of a transonic airfoil based on particle image velocimetry, Measurement Science and Technology 20 (2009) 074005. Doi:10.1088/0957-0233/20/7/074005.

74 T. Lee, Y. Y. Su, Low reynolds number airfoil aerodynamic loads determination via line integral of velocity obtained with particle image velocimetry, Experiments in Fluids 53 (2012) 1177–1190. Doi:10.1007/s00348-012-1353-x.